Particle-turbulence interaction of high Stokes number irregular shape particles in accelerating flow: a rocket-engine model

Sabrina Kalenko[a], Alexander Liberzon[a]

[a] *Turbulence Structure Laboratory, School of Mechanical Engineering, Tel Aviv University, Tel Aviv 69978, Israel*

Abstract

Metal particles in solid propellants enhance rocket engines performance. An interaction of particles with a high Reynolds number turbulent gas flow accelerating to a nozzle, has not been characterized thoroughly. We study the particle-turbulence interactions in a two-dimensional model of a rocket engine. Two-phase particle image/tracking velocimetry provides the flow velocity simultaneously with the velocities of irregularly shaped inertial particles ($d_p \sim 350\mu$m, Stokes $St \sim 70$, particle Reynolds number $Re_p \sim 300$). We reveal the local augmentation of turbulent fluctuations in the particle wakes (up to 5 particle diameters downstream the particle). Despite the low mass fraction, the large response time of the particles leads to an increase of turbulent kinetic energy (TKE) everywhere in the chamber. The increase of local particle mass fraction near the nozzle, due to the mass conservation and converging streamlines, compensates for the dampening effect of the strong mean flow acceleration and further augments TKE at the nozzle inlet. Furthermore, this is accompanied by unexpectedly isotropic fluctuations in the proximity of the nozzle. The phenomenon of the isotropic, strongly enhanced turbulence in the proximity of the engine nozzle achievable with the low mass fraction of high St, Re_p particles, can be used to improve the design of solid propellant rocket engines.

Keywords: Particle laden turbulent flow, Rocket engine, Turbulence modulation, Spatial acceleration

---

1. Introduction

Despite a vast body of research on the dynamics of dispersed particles in turbulence, we cannot predict whether TKE will be augmented or attenuated in complex flow cases (Balachndar and Eaton, 2010). For instance, apparently similar flow cases were reported to have contradicting trends in studies of particle-turbulence interaction in fully developed channel flows for different sizes and densities of particles Kulick et al. (1994); Kussin and Sommerfeld (2002); Kiger and Pan (2002); Li et al. (2012). Kulick et al. (1994) investigated turbulent flow in a vertical channel and found turbulence attenuation that increased with mass loading and Stokes number. Kiger and Pan (2002) showed turbulence augmentation far from the wall and negligible effect near the wall. Kussin and Sommerfeld (2002) found significant turbulence augmentation near the channel center plane for particles larger than η with particle Reynolds numbers above 350, and turbulence attenuation near the wall. Conversely,Li et al. (2012) found increased fluctuations near the wall and reduced fluctuations in the outer region of the boundary layer. Cisse et al. (2013) developed a fully resolved direct numerical simulation around a relatively large particle at moderate particle Reynolds numbers, and using conditional analysis in the coordinate system relative to the particle position, have shown that particles reduce fluctuations in their wake. The authors presented particle fluid coupling at distances of one particle diameter and that a particle essentially creates a "shadow in its wake". At larger particle Reynolds numbers, Hetsroni (1989) found an augmentation of TKE. The authors explained this by the vortex shedding mechanism in the wake of the particle. These examples are by no means a comprehensive review of the existing literature. It is a small sample emphasizing that a small variation of parameters, along with the carrier phase flow and particle properties, can produce substantially different effects of particles on the TKE.

Particle-fluid flow interaction is characterized by the ratios of a) length scales, namely, the size of the particle relative to the relevant flow length scale, b) time scales, i.e., particle response time relative to the relevant flow time scale, or the Stokes number, c) particle Reynolds number, Re_p, based on the relative (sometimes called slip) velocity (Hetsroni, 1989; Tanaka and Eaton, 2008):

$$Re_p = \frac{|\boldsymbol{U} - \boldsymbol{V}_p| d_p}{\nu}, \tag{1}$$

where d_p is the particle diameter, $\boldsymbol{V}_p$ is the particle velocity (bold symbols denote vectors), ν is the fluid kinematic viscosity, and $\boldsymbol{U}$ is a so-called "undisturbed fluid velocity at the position of the particle", which is practically estimated as an interpolation of the surrounding fluid velocity to the position of the particle (e.g. Meller and Liberzon, 2015). The particle relaxation time τ_p for small and relatively heavy particles, $\rho_p \gg \rho_f$ and $Re_p < 1$ is defined as:

$$\tau_{p,s} = \frac{\rho_p d_p^2}{18\mu} \tag{2}$$

However, for higher Re_p a non-linear drag force correction is required (Crowe et al., 2011):

$$\tau_p = \frac{\tau_{p,s}}{1 + 0.15\, Re_p^{0.687}} \tag{3}$$

The Stokes number is the time scales ratio (Crowe et al., 2011):

$$St = \frac{\tau_p}{\tau_f}. \tag{4}$$

Large Stokes number $St \gg 1$ means that particles response time is longer than the flow time scale. In this work, the particles are larger than the Kolmogorov length scale ($d_p > \eta$), and heavier than the surrounding fluid ($\rho_p \gg \rho_f$). Therefore, an appropriate flow time scale is that of the mean flow, i.e., $\tau_f = L/U$, where L is a turbulent integral scale.

The length scales ratio, d_p/L, where L is the integral length scale of turbulence, was proposed by Gore and Crowe (1989) to distinguish between attenuation for $d_p/L < 0.1$ and augmentation for $d_p/L > 0.1$.

Separately, the aforementioned ratios of time/length scales could not predict reliably the augmentation or attenuation effect for different flow cases. Tanaka and Eaton (2008) suggested another dimensionless parameter that combines the Stokes number with the flow Reynolds number $Re_L = UL/\nu$ and turbulence scale separation η/L:

$$Pa = St\, Re_L^2\, (\eta/L)^3 \tag{5}$$

The authors (Tanaka and Eaton, 2008) combined empirical data from 80 experiments and demonstrated that in the range $10^3 < Pa < 10^5$ there is an attenuation of TKE, while for all other cases (below 10^3 or above 10^5) there is an increase in TKE due to particles.

Gany et al. (1978) photographed aluminized solid propellants under cross-flow conditions forming and burning in the form of agglomerates of Al/Al_2O_3. The primary particles of the order of 10 μm behaved like flow tracers and did not exhibit two-way coupling. However, the irregularly shaped agglomerates, in the range of 40 to 800 μm, that formed primarily on the surface during the burning process, afterwards were detached and carried by the turbulent flow. Caveny and Gany (1979) studied the breakup of agglomerates in aluminized propellants when the agglomerates burn slowly compared to the residence time in the rocket motor. They found that the agglomerates velocity lags in the nozzle, cause breakup of sufficiently large agglomerates, and thereby permit reasonable combustion efficiency to be achieved. The motion of large irregular particles resembling the agglomerates in the turbulent flow and their contribution to the TKE balance (augmentation vs attenuation) is the central question of this study.

In this work, we study experimentally the effect of large, heavy, and irregularly shaped particles on the TKE in a simplified model of a rocket engine. We reproduce the key features of the mean flow: a) acceleration towards the nozzle; b) the shape of the chamber and the converging type of flow through a small nozzle throat; and c) particle sizes that correspond to metal agglomerates reported in the literature. In this flow, there are competing effects of acceleration, particle-turbulence interaction, and monotonically increasing local mass fraction due to the contracting flow through the nozzle. To what extent various mechanisms contribute to the overall increase or decrease of turbulent kinetic energy is not yet clear.

This two-phase flow case is somewhat different from the aforementioned ones also in the sense that the particle residence time in the flow is rather short as compared to the particle response time. Due to fluid acceleration towards the nozzle, all the key parameters, the relative velocity, Stokes number, particle Reynolds number, the fluid Reynolds number, all vary in the Lagrangian sense, or inhomogeneous in the Eulerian sense. The case is to some extent analogous to the interaction of large Stokes particles with the near to far-field of the jets (Prevost et al., 1996), but all the changes occur on time scales shorter than the particle residence or response time.

We used particle image/tracking velocimetry (PIV/PTV) to measure simultaneously the velocities of the fluid and particulate phases in two dimensions. In the most general case, a two-wavelength illumination and imaging would be necessary to distinguish between the two phases (Elhimer et al., 2017; Poelma et al., 2006). However, in this case the particles are much larger as compared to the flow tracers, and a simple PIV system is sufficient to separate the particles and fluid tracers (Khalitov and Longmire, 2002; Hwang and Eaton, 2006). Simultaneous measurements allow to estimate the instantaneous slip velocity using local flow interpolation and to measure TKE, as well as its change in respect to the location of particles.

2. Experimental details

We created a quasi-two-dimensional experimental chamber (500 mm long, 245 mm wide, and 35 mm front-to-back wall distance, nozzle throat width is 35 mm) which resembles a cross-section of a generic solid-propellant rocket motor with round symmetrical cavities (Volkov et al., 2012; Ciucci and Iaccarino, 2012), shown in Fig. 1. The cavities are characteristic of solid rocket motors with a thrust vectoring system. The back and front walls of the channel were made from glass for particle imaging and the side walls have optical windows to enable optical access for the laser sheet. The purpose is to create a quasi-two-dimensional velocity field as a proxy of the two-dimensional axisymmetric flow field in a cylindrically shaped rocket engine.

The chamber was positioned vertically with the main flow direction and the particle motion aligned with the gravitational acceleration (Fig. 1a). The air was supplied by a blower through a converging channel (750 mm above the measurement region). The measurement volume is 70 $\times$ 63 mm, the lowest edge is 40 mm above the nozzle entrance, as shown in Fig. 1b. Above this measurement location, the flow resembles the fully developed channel flow with constant streamwise velocity. Within the measurement, the region flow is spatially changing in both streamwise and spanwise directions, accelerating and converging into the nozzle. as shown in Fig. 1b.

Olive oil aerosol (1 μm droplets) produced by a Laskin nozzle seeder, and alumina particles supplied by a custom-made particle seeder (both manufactured by I.T.E.S Engineering LLC, Israel) were mixed into the air stream before entering the chamber.

We measured turbulent flow and particle motion for two flow rates (low/high). The Reynolds number at the throat is based on the characteristic velocity defined by the volumetric flow rate through the chamber and the cross-sectional area of the nozzle. The Reynolds number at the throat is $Re_L = 185,000$ and

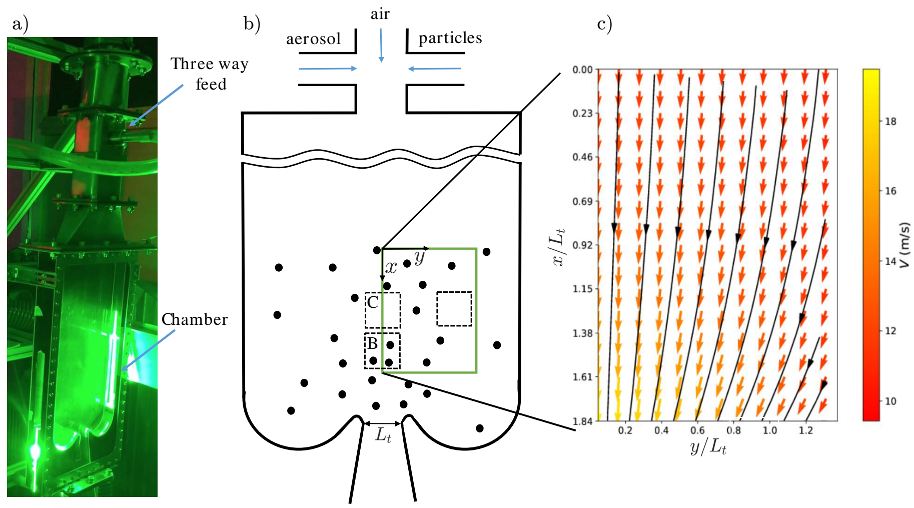

Figure 1: a) Photograph of the experimental system, b) Schematic side view diagram of rocket engine model and PIV setup and picture of the experimental setup. The coordinate system is defined with x in the direction of the mean flow through the nozzle and y is the transverse direction, the origin is at the nozzle throat. c) Ensemble average velocity field and streamlines in the measurement region of 140 $\times$ 150 mm.

$260,000$, for the low and high flow rates, respectively. In our setup, L_t is the size of the nozzle throat, and the smallest dimension of the chamber determines the integral scale of the turbulent flow. Additional relevant parameters for the two experiments are given in table 1.

The PIV setup consists of the double-head pulsed Nd:YAG laser (120 mJ/pulse, 532 nm, 15 Hz, New Wave Solo), with laser optics creating a light sheet with approximately 1 mm wide, and a 2672 $\times$ 4008 pixel double exposure 12 bit CCD camera (TSI Inc. Shoreview, MN), equipped with a 100 mm Nikon macro-lens at f/2.8, resulting in a spatial resolution of 42 μm/pixel.

For the PIV analysis, we used Insight 3G software (TSI Inc.) and compared it to the open source software (OpenPIV, 2019). We used a multi-pass algorithm from 64 $\times$ 64 to 32 $\times$ 32 pixel interrogation windows, with 50% overlap. The multi-pass method increases the dynamic range, which is especially important for the particle-laden flow cases, due to the high relative (slip) velocity. At each iteration, the outliers vectors were rejected and replaced by the mean of the five nearest neighbors. The experiments consist of 4 runs at two flow rates with/without particles. Every experimental run consists of 5 sets (repetitions), 125 pairs of images each.

The mean flow in the region of interest is shown qualitatively in Fig. 1c as color-coded vector plot and streamlines. The spatial coordinates x and y are normalized by the nozzle width L_t. Note that the position of the region of interest is shown in Fig. 1b. The bottom side is one nozzle throat length away from the nozzle entrance. The streamlines of the flow field for both Reynolds

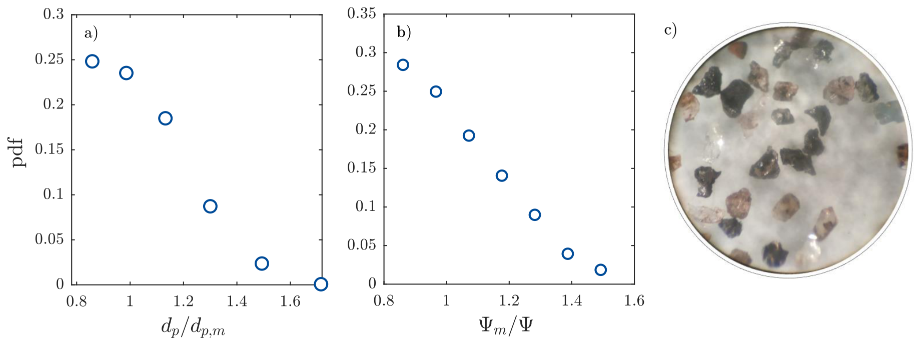

Figure 2: a) Probability density function (PDF) of particle effective diameters d_p defined as a diameter of an equivalent sphere and normalized by the effective mean diameter $d_{p,m}$ of 320 μm b) PDF of reciprocal of sphericity Ψ^{-1} normalized by the mean shericity Ψ_m^{-1} c) alumina particle's picture under a microscope.

numbers are practically identical, except for the representative velocity scale at the nozzle throat of 96 m/s for the low flow rate and 135 m/s for the high flow rate experiments.

2.1. Particles

We used non-spherical alumina particles that are common in solid propellants for rocket engines and other industrial applications. An effective particle diameter d_p was measured with a laser diffraction device (Malvern Analytical) and presented in Fig. 2a. In Fig. 2b, we present the reciprocal of the inscribed circle sphericity of the particles (Wadell, 1935; Riley, 1941), the square root of the ratio of the inscribed and circumscribed circles of the particle. The particle distribution cut off below 250 μm because the particle was separated from coarser particles with a 250 μm sieve. The mean sphericity of 56 particles, examined under a microscope, is $\Psi_m = 0.81 \pm 0.1$. The microscopic images are shown in Fig. 2c, emphasizing random shapes, sharp edges, rough surfaces, cavities, and protrusions.

In table 1, we present the flow and particle parameters (some are given as the range of values in the chamber) for the two experiments. Using PIV data and the aforementioned definitions in Eqs. (2) – (4), we estimated the particle response time scales and the Stokes number. The residence times of the particles, estimated from $\tau_r = H/V_p$ when H is the height of the chamber and V_p in the mean particle velocity, were 30 to 40 ms. The ratio of particle response time to the residence time, τ_p/τ_r, is between 2 and 4, for the two Reynolds number runs. This ratio explains that particles leave the chamber before they can respond to the air streamwise velocity.

Furthermore, we estimate the response of the particles to the spatial acceleration of streamwise velocity using the acceleration time scale, τ_a:

$$\tau_a = (dU_c/dx)^{-1} \tag{6}$$

and the ratio of scales, τ_a/τ_p. Mean slip due to acceleration of the flow is expected when $\tau_a/\tau_p > 1$. In our flow, however, $\tau_a/\tau_p \ll 1$ is everywhere in the chamber (table 1). Thus, these particles can be characterized in general as "unresponsive" (Hardalupas et al., 1989). It is also important to mention that when $\tau_a/\tau_p = 1$, there is a mean slip for finite-size particles due to the shear across the particle diameter.

The time scale ratios do not mean that there is insignificant local particle-turbulence interaction. Conversely, there is a substantial transfer of momentum between the particulate phase and the turbulent fluctuations of the carrier flow, as will be explained in the following.

Table 1: Particle and flow parameters: Re_L based on flow rate, τ_p is the particle response time, Eq (3), τ_a is the flow acceleration time scale, Eq. (6), τ_r is the particle residence time estimated from $\tau_r = H/V_p$ when H is the height of the chamber, t_f is the integral time scale, $t_f = L_t/U_f$, St is the Stokes number, Eq. (4), τ_a is the acceleration time scale, Eq. (6), particle Reynolds number, Eq. (1), L is the integral length scale based on the autocorrelation function and η is the Kolmogorov length scale $\eta = (\nu^3/\epsilon)^{1/4}$, when ϵ is the dissipation derived from the structure function.

Exp.	Re_L	τ_p (ms)	τ_a (ms)	τ_r (ms)	t_f(ms)	S_t	τ_p/τ_r	τ_a/τ_p	Re_p	L (mm)	η (μm)
1	260000	75-90	0.1-1	30	9-11	85	2-3	0.0013- 0.011	300-450	9	62
2	185000	95-121	0.2-3.4	40	13-15	75	2-4	0.0021-0.028	450-650	9	76

2.2. Two-phase PIV/PTV velocity analysis

We follow the procedure previously reported by Khalitov and Longmire (2002), among others. We filter PIV images based on the size and intensity of objects, (above 15 pixels in diameter and intensity level of 200/255) to create particle-free PIV images from which we obtain turbulent velocity fields. The separated images of large particles processed with particle tracking velocimetry (PTV) analysis, using the nearest neighbor algorithm are written in Matlab (Mathworks Inc.). In Fig. 3, we present an example of a small region in an instantaneous flow field (green arrows overlaying the original image) of the carrier phase and particulate phase on the left panel, and the fluctuating flow field in the right panel (after subtracting the ensemble averaged flow field, shown in Fig. 1c.)

3. Results

In this section we will summarize the main results obtained from the two-phase PIV/PTV measurements. We present first the definition of the local mass loading ratio, describing the ratio of particles mass to the mass of air, varying with the distance to the nozzle. The mass distribution is not uniform in the flow field and this fact is reflected in the the flow field results. We proceed to the comparison of the mean and turbulent flow profiles for unladen versus particle-laden flows and conclude the results section with the local analysis of particle-turbulence interactions.

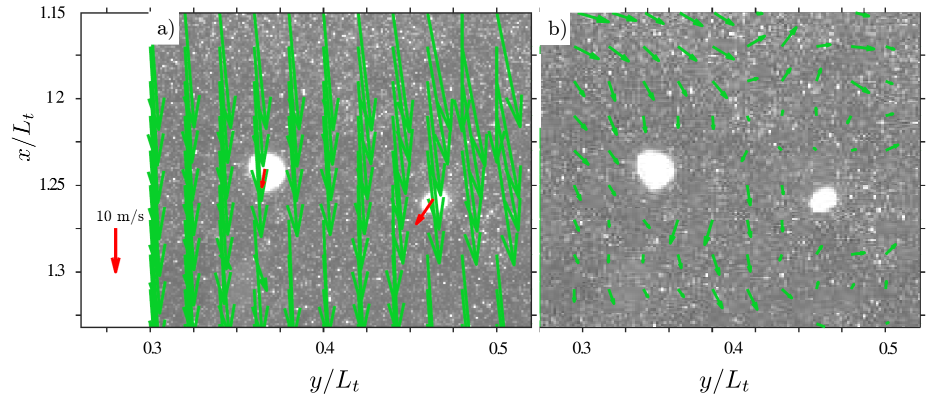

Figure 3: Instantaneous flow field of the carrier phase in the green vectors and particulate phase in the red vectors; a) for instantaneous flow field; and b) for the fluctuations, overlapped on the original PIV image. The flow field was taken from the dashed square in Fig. 1.

3.1. Local mass loading ratio

The mass fraction or mass loading ratio, ϕ, is defined as the ratio of particle mass in respect to that of the fluid. We estimate the local mass loading at various distances from the beginning of the measurement volume based on the number of particles, N, extracted from PIV images, and their size distribution, shown in Fig. 2a. The mass of particles is divided by the mass of air in the measurement volume. This volume is calculated as the area of interest in the PIV image times the laser sheet thickness, excluding the volume of particles within the measurement volume. The thickness of the laser, obtained from the reflection of the laser from a calibration target inside the measurement section. The reflection was recorded with the high magnification PIV camera and estimated to be approximately 1 mm. The volume of the particles we estimate using their equivalent diameter of 320 μm, obtained as the weighted mean from the probability distribution in Fig 2a. We estimate the errors due to spatial inhomogeneity, laser sheet thickness non-uniformity, and particle size distribution approximations to sum up to 10%. The corresponding volume fractions are $\langle \phi_v \rangle = 3.7 - 7.4 \times 10^{-5}$ for the low flow rate and $0.1 - 0.3 \times 10^{-5}$ for the high flow rate, respectively. The volume loading range corresponds to the two-way coupling regime, (Elghobashi and Trusedell, 1993), far from the four-way coupling regime $\langle \phi_v \rangle > 10^{-2}$. Although recent computational studies (Esmaily and Horwitz, 2017) have shown that even at low volume fractions there is a possibility of inter-particle interactions, we could not find any evidence of such interactions in the results.

We present the local mass loading ratio, averaged from the ensemble of PIV images, and horizontally across the measurement volume, $\langle \phi \rangle$, in Fig. 4a. Note that the streamwise flow direction is from small x/L_t to large x/L_t, and the mass loading ratio increases as the flow with particles approaches the nozzle. The particles trajectories converge with the flow towards the nozzle and the mass loading increases because of the conservation of mass. The mass loading of the particles could not be precisely controlled in the present setup, as the particles enter the air flow from a pneumatic seeder that was kept at constant pressure and flow rate. This experimental artifact leads to a higher particle entrainment rate and the higher on average mass loading, mass loading for the lower air flow case. Accordingly, a larger number of particles in the chamber lead to a steeper mass loading increase rate as the flow accelerates towards the nozzle.

It should be noted that due to the two round cavities on both sides of the chamber from which particles rebound at high speed, few particles arriving at a large angle to the streamwise direction were excluded from the present data.

3.2. Mean air and particle velocities

In Fig. 4b, we plot the variation of the average streamwise velocity along the centerline, U_c (hereinafter capital letters denote the ensemble averaged quantities, lower case letters for turbulent quantities) for the particle unladen (filled triangles) and laden cases (open circles) for the two Reynolds numbers (different colors). In addition, we plot the average velocity of particles (squares). In the lower panel, Fig. 4c-d, we present the mean velocity profiles (unladen and laden flow cases) at several distances from the nozzle for a more quantitative presentation of the flow field. The summary of the key flow features visible in Fig. 4b-d is:

- the mean streamwise velocity rapidly increases towards the nozzle (Fig. 4b-c) with spatial acceleration values of $\partial U/\partial x \approx 2,000 - 10,000$ s^{-1});
- The flow accelerates spatially also in the transverse direction, from the sides of the measurement volume towards the centerline, with $\partial U/\partial y \approx 500 - 3,000$ s^{-1} (Fig. 4d);
- average particle velocities, V_p are practically constant during the time particles cross the measurement volume (squares at the bottom of Fig. 4b);
- the average air velocity distribution and amplitude have not changed in particle-laden cases as compared to the unladen ones (the filled and open symbols in Fig. 4b-d) ;
- the high Stokes/Reynolds number irregular inertial particles move significantly slower than the air flow and preserve their velocity (squares in Fig. 4b), despite substantial flow acceleration.

The particles do not have enough time to respond to a spatial streamwise velocity gradients, despite a strongly accelerating flow. This result is in agreement with the experiments of Gilbert et al. (1955) and Gany et al. (1978); Caveny and Gany (1979), where agglomerates of $200 \div 1000\,\mu$m were found to move slower as compared to the carrier flow everywhere in a two dimensional rocket motor chamber.

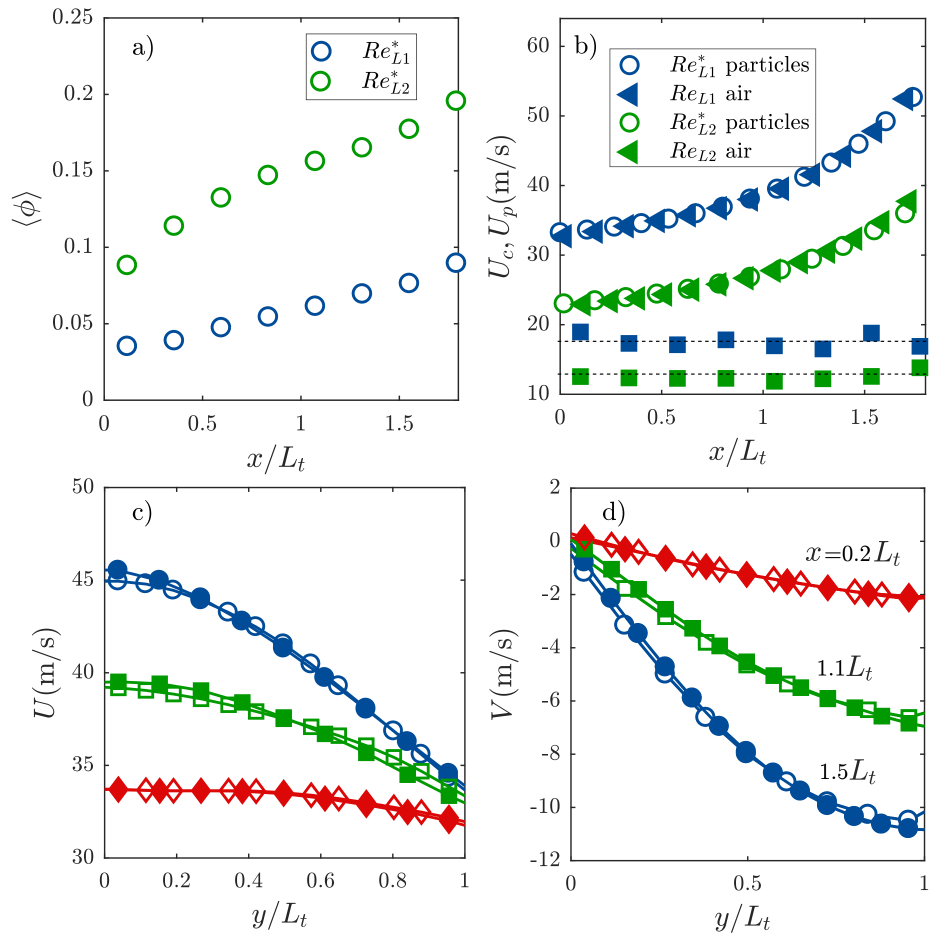

Figure 4: a) Averaged mass loading $\langle\phi\rangle$ along the centerline. Superscript * denotes the particle laden cases. x/L_t b) Air mean air flow velocity along the centerline of the chamber, U_c and particles average streamwise velocity U_p. Triangles are for the unladen cases, open circles for the particle laden cases (in both panels). Square markers are for the particle velocity U_p. c-d) Mean velocity profiles, $U(y)$ and $V(y)$, respectively, for the un-laden (filled) and laden cases (open symbols) at Re_{L1}, at different distances from the nozzle, $x/L_t = 0.5, 1.3, 1.7$ (diamonds, squares and circles, respectively).

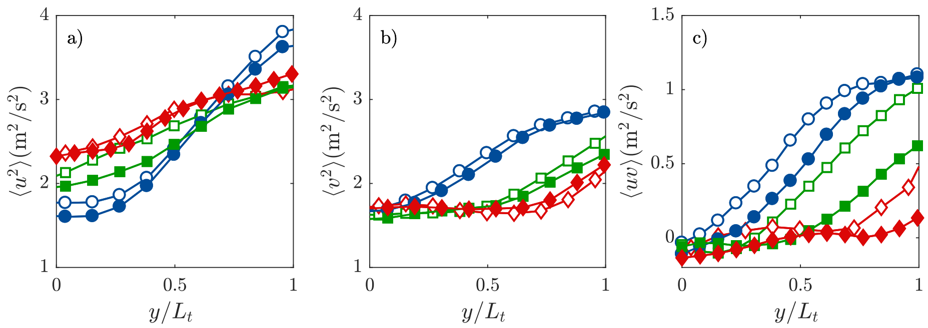

Figure 5: Turbulent kinetic energy component profiles a) $\langle u^2 \rangle$, b) $\langle v^2 \rangle$ and c) $\langle uv \rangle$, respectively, for Re_{L1} and the un-laden case (filled symbols) and laden case (empty symbols). The symbols and colors legend are the same as in Fig. 4.

3.2.1. Turbulent kinetic energy, Reynolds stresses and production

In Fig 5a-c we present the profiles of turbulent kinetic energy (TKE) components: streamwise $\langle u^2 \rangle$, transverse $\langle v^2 \rangle$ and the Reynolds stress component $\langle uv \rangle$ for the Re_{L1} unladen flow case. We present profiles at the same distances from the nozzle as for the mean flow profiles in Fig. 4c-d.

First, we observe from the spatial distributions that the fluctuations are stronger at the sides (large y/L_t), far from the centerline. The strong reduction of turbulent kinetic energy at the centerline is due to the acceleration. Furthermore, the acceleration affects differently the streamwise component (decreasing) and the transverse component (increasing on the sides and constant at the centerline shown by the order of the profiles from diamonds to circles (from $0.5L_t$ to $1.5L_t$, respectively). We also observe that the Reynolds stress values are large far from the centerline. At the centerline, partially due to symmetry and partially due to acceleration, the Reynolds stresses are practically zero. These results are in agreement with the modification of the turbulence structure observed in converging channels, see, for instance Shah and Tachie (2008).

We combine the results from the ensemble averaged flow fields and the turbulent properties to estimate the terms of turbulent kinetic energy production in Fig 6a-d. We plot the profiles of turbulent production terms $\langle uv \rangle \frac{\partial U}{\partial y}$,$\langle uv \rangle \frac{\partial V}{\partial x}$, $\langle u^2 \rangle \frac{\partial U}{\partial x}$, and $\langle v^2 \rangle \frac{\partial V}{\partial y}$, for the unladen and laden cases (filled and open symbols, respectively) at Re_{L1} (at the same distances from the nozzle as in Fig 5).

The effects of acceleration on the TKE production Fig 6a-d are visible in the terms $\langle uv \rangle \frac{\partial U}{\partial y}$ and $\langle uv \rangle \frac{\partial V}{\partial x}$. The terms contribute positively to the TKE production far from the centerline with the peak at about $x/L_t \approx 0.5$, and decrease towards the centerline. This is partially due to symmetry of the flow and diminishing derivatives $\partial U/\partial y$ and partially due to the decorrelation of the velocity components. Along the centerline ($y = 0$), the intense spatial acceleration towards the nozzle and TKE components u^2 and v^2 contribute to a sort of "negative TKE production". It is noteworthy that the two terms $\langle u^2 \rangle \frac{\partial U}{\partial x}$ and $\langle v^2 \rangle \frac{\partial V}{\partial y}$ in Fig 6c-d are also stronger as compared to the production terms stemming from the Reynolds stresses in Fig 6a-b. On the overall, it can be summarized that the strong spatial acceleration in the streamwise and transverse directions due to the convergent type of the flow diminishes TKE production terms, therefore the turbulent fluctuations in the unladen flow case decrease towards the nozzle.

3.3. Particle-turbulence interaction mechanism

Figures 4b-d, 5a-c, and 6a-d present the effects of particles on the mean flow, TKE components and the TKE production terms, respectively. We noted that the mean flow in the chamber has unchanged insignificantly and the small variations of a few percents appear closer to the nozzle. The centerline velocity profiles along x and the transverse profile (e.g., $U(y)$) all show that the flow velocity field is practically unchanged at the same locations with only a slight reduction of the mean velocity in the particle-laden case (the results for the lower Reynolds case are similar and not shown here for the sake of brevity). We observe somewhat increasing fluctuating components in Fig. 5a-b, however, the most prominent change is in the field of Reynolds stresses in FIg. 5c. Clearly, this increase also affects the production terms shown in Fig. 6a-b. However, because of the strong acceleration, the negative TKE production terms are dominant and increase towards the nozzle entrance.

We also recall that the flow is in the dilute two-way coupling regime, with a relatively small number of heavy particles. Therefore, in the following we present a more insightful, local analysis around the particles and as a function of distance from the particles.

To reveal the local effects of particles on the turbulent flow, we use conditional sampling in the following form: we divide the instantaneous PIV/PTV fields in the particle-laden cases, along the centerline, into small control volumes of 20×20 mm. From each sub-volume, we conditionally sample the turbulent fluctuations depending on whether the sub-volume in a given flow realization contains particle(s) and marked it as a region B (particles) or C (no particles) (as schematically marked in Fig. 1a). For the sake of reference we compare with the distributions of properties in case A that is the clear air flow case at the same Reynolds number and at the same sub-volume locations.

In Fig. 7, we present a comparison of probability distribution functions (PDF) of the streamwise fluctuations in the case of a unladen flow case (red triangles) with these at two conditional samples: the regions with at least one particle (B) and the regions in the particle-laden case that do not contain inertial particles (C). Both PDFs of the particle-laden cases have wider tails, corresponding to higher u' values (up to 3 times higher values, as seen in Fig. 7b.) The turbulent flow in the proximity of the inertial particles (case B) is significantly different from the unladen case (case A). It is noteworthy that the turbulent fluctuations are stronger also far from the particles (case C), as if the flow is "contaminated" with the velocity fluctuations stemming from the local particle-turbulence interactions. The result are a different view on the increase of fluctuations in particle-laden case, shown above in Fig. 5.

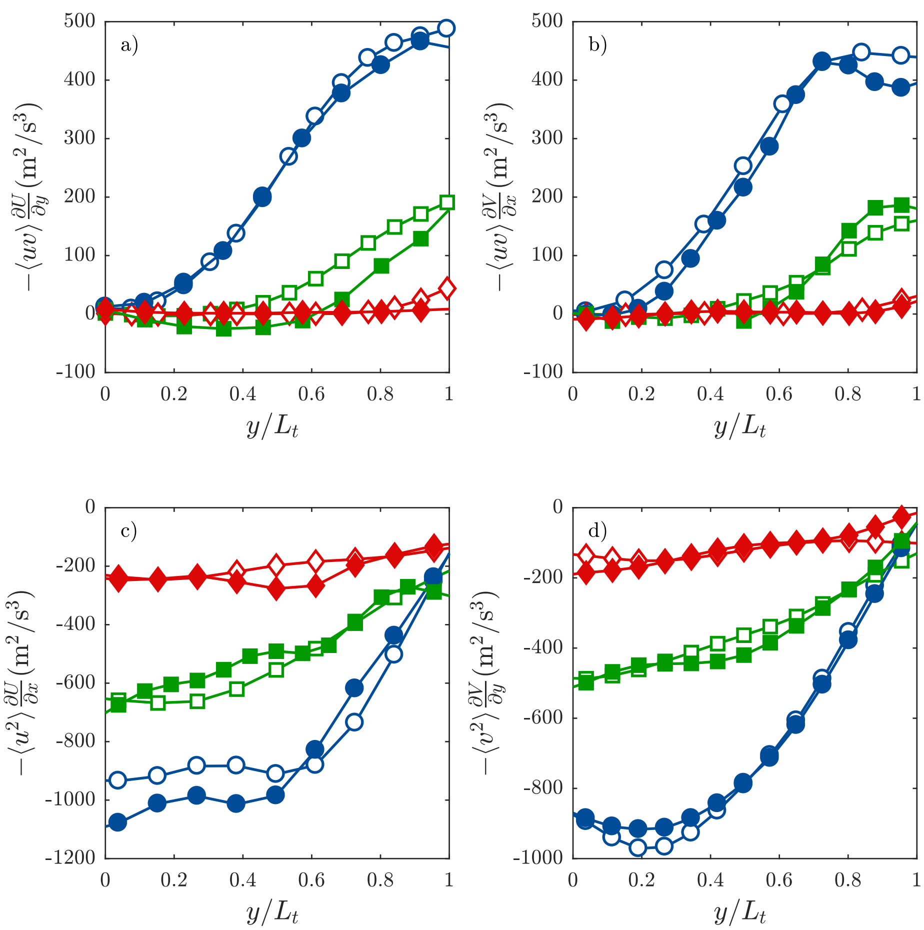

Figure 6: Profiles of turbulent production terms: a) $\langle uv \rangle \frac{\partial U}{\partial y}$, b) $\langle uv \rangle \frac{\partial V}{\partial x}$, c) $\langle u^2 \rangle \frac{\partial U}{\partial x}$, and d) $\langle v^2 \rangle \frac{\partial V}{\partial y}$, respectively, for the un-laden case (filled symbols) and laden case (empty symbols) and for Re_{L1}, at different distances from the nozzle. The symbols and colors legend is the same as in Fig. 4.

Reflecting on the introductory section, we can attribute these local effects with negative fluctuations to the "vortex shedding" regime and infer that the wakes are transported and affect the flow for a substantially longer time scale as compared to the particle residence time. To quantify the region of influence of particles on turbulent fluctuations, we present in Fig. 7b the r.m.s of streamwise fluctuations (denoted by u') in particle-laden cases normalized by the value of the unladen cases for the two Reynolds numbers. For this plot, we sample PIV flow realizations in respect to the particle centroids in the streamwise direction (i.e., in the Lagrangian frame of reference attached to the particle center). The normalized r.m.s. of streamwise fluctuations in the particle wake is plotted versus the streamwise distance from the particle, normalized by the particle average diameter, d_p (downstream, in the direction of motion of the particle). We observe significantly higher turbulent fluctuation within a region of at least 5 diameters and the effect of slightly increased turbulent fluctuations far from the particle, supporting the aforementioned results in terms of distributions in Fig. 7a or profiles in Fig. 5a-c.

We are also interested in the local analysis of the effect of decorrelation on the streamwise and transverse fluctuations observed in Fig. 5c. The results of the conditional sampling analysis along the centerline are shown in Fig. 8. We present the values of u' and v' of the local/non-local conditional samples and of the unladen case together to emphasize the different rate of decrease of the fluctuations in the direction of mean flow acceleration. The ratio of r.m.s. of the fluctuations v'/u' which is in some sense a measure of anisotropy (a horizontal line at $v'/u', = 1$ means the isotropic ratio of fluctuations) is shown in Fig. 8b.

The local analysis reveals very peculiar phenomena arising due to the competition between the effect of strong acceleration (namely, a strong decrease of streamwise fluctuations and an increase of spanwise fluctuations), and the effect of the particles, which increase the fluctuations locally in the downstream wake of the particle. The peculiarity is that the two counteracting effects lead to an isotropic ratio of turbulent fluctuations. We recall that the effects are linked to the local mass fraction increasing towards the nozzle, as was shown in Fig. 4a.

4. Summary and conclusions

In this work, we created the experimental setup of a two dimensional model of a rocket engine and studied the particle-turbulence interaction when the particulate phase consists of dispersed alumina particles of irregular shape in the size range of $250 - 550\,\mu$m. We focused on the pre-nozzle region in which the carrier phase flow spatially accelerates towards the nozzle. We applied a two-phase PIV/PTV algorithm and quantified the carrier and particulate phase velocity fields.

The alumina irregularly shaped particles are strongly inertial with relatively high Stokes and particle Reynolds numbers. The particles pass the finite size flow chamber quickly, as compared to their response time scale. As a consequence, the interactions are abrupt and strong, but the residence time is much shorter as compared to the particle response time. Therefore, in this peculiar

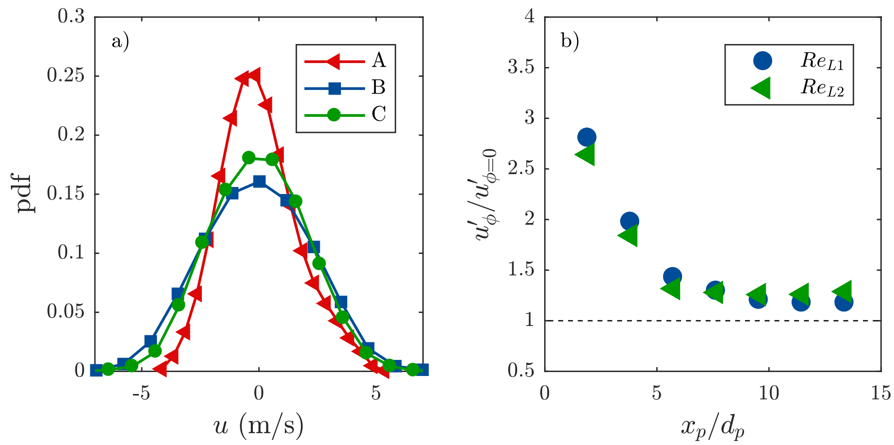

Figure 7: a) PDF of streamwise velocity fluctuations at $x/L_t \approx 1$ along the centerline, $y = 0$, where the red triangles denote the unladen case (A), blue squares denote the particle-laden flow with instantaneous accumulation of particles (B) and the green circles denote the particle-laden flow with locally clear air (C). Skewness values are 0.25, -0.11 and 0.48, respectively. b) Root-mean-square of streamwise fluctuations u' for the particle laden cases at two Reynolds numbers as a function of distance from the particle, normalized by the corresponding r.m.s of the unladen flow case. The distance is measured along streamwise direction from the origin attached to the particle, x_p, normalized by the mean particle diameter.

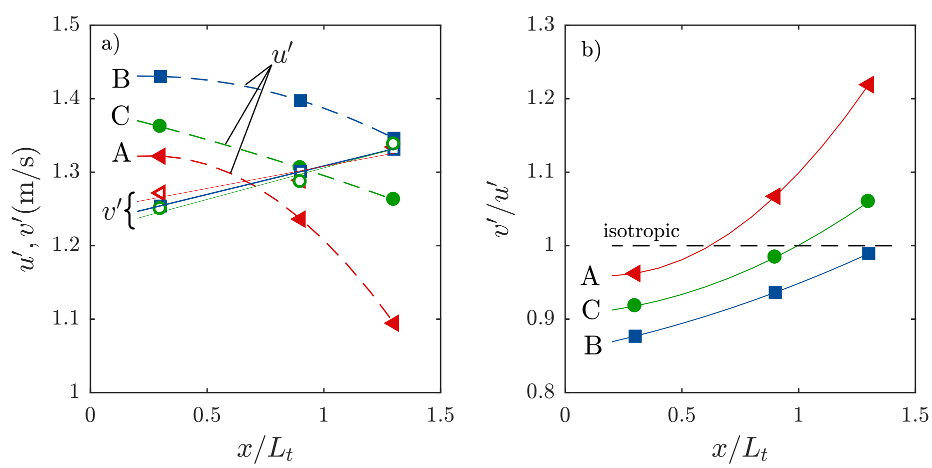

Figure 8: a) Root-mean-square of fluctuation components, v' and u' along the centerline x/L_t (same legend as in Fig. 7). Filled markers denote u' and open markers are for v'. b) anisotropy measure, v'/u' for the three cases A-C, a horizontal line at $v'/u' = 1$ emphasizes the isotropic ratio.

situation, the particles move at almost constant average velocity, despite the fact that the carrier phase flow rapidly accelerates towards the nozzle. This leads to the high and monotonically increasing relative (slip) velocity between the particulate phase and carrier flow.

The combination of the high particle-fluid relative velocity, slow response time, and rapid acceleration of the air mean flow leads to substantial turbulence argumentation, mostly in the streamwise component. The particle-related mechanism for these Stokes numbers range from $St > 75$ and the particle Reynolds numbers $Re_p > 300$ were termed in the literature as "vortex shedding" mechanism Hetsroni (1989); Balachndar and Eaton (2010). In the present case, in particular, the particles move slower than the carrier fluid flow. Thus, a turbulent wake, a region where the flow slows down, is in the direction of relative velocity, which defined as $\vec{V}_r = \vec{U}_f - \vec{V}_p$. The wake region "downstream" in respect to the particle. It means that the next particle position will be inside the wake of the particle itself at the previous time instant. More detailed local flow around the particles analysis shows that on average, a local reduction of the air flow velocity in the particle wake is pronounced up to five particle diameters downstream from the particle. We presented the comparison of the local turbulence augmentation in the proximity of the particles and compared it to the turbulence augmentation in the entire region of interest. We also demonstrated the peculiar situation of streamline convergence leading to an increase of the local mass fraction, streamwise acceleration, and particle-turbulence interactions. First, the streamwise average velocity acceleration significantly reduces the streamwise turbulent fluctuations. Second, inertial particles of irregular shape create streamwise fluctuations in their wakes due to the vortex shedding and compensate the mean flow acceleration effect. In addition to the dramatic increase of TKE, the particle wakes are unexpectedly more isotropic than the surrounding turbulence. Furthermore, the particle wakes are much more isotropic as compared to the unladen flow case with the mean flow acceleration.

In our experiment, the particle mass fraction is monotonically increasing towards the nozzle due to mass conservation and streamlines convergence (see 4). Nevertheless, in the measurement region of interest, the mass fraction is in the two-way coupling regime and we did not observe any clustering of particles. Our conclusions are therefore, limited to the dilute two-way coupling regime.

In respect to the aforementioned particle-flow dimensionless parameters, we have estimated that $P_a > 10^5$ in the entire measurement region. As suggested by Tanaka and Eaton (2008), it falls in the range that predicts an increase in turbulence. The length scales ratio, d_p/L (Gore and Crowe, 1989) is lower than 0.1 and predicts attenuation, however our particles lead to augmentation. This discrepancy is likely to reflect the fact that the main effect is due to the particle wakes that are five times larger than the particle effective diameter.

This empirical work does not improve significantly our ability to predict the effects of particle-turbulence interactions in a general case. However, it adds a few important observations relevant for the case of particle-laden flows with high Stokes/Reynolds numbers irregularly shaped particles, especially in the case of accelerating and converging incompressible flows. We demonstrate the mechanism by which a small mass fraction of particles in the accelerating and converging flow leads to up to 20% increase of turbulent kinetic energy (at $x/L_t = 1.5$ in Fig. 8.a)). It could lead to a comprehensive choice of the particle shape and density (St, Re_p) and the mass fraction (number of particles per volume of solid propellant) that can compensate the decrease of TKE by the flow acceleration. Furthermore, we demonstrate that irregularly shaped particles, moving more slowly than the surrounding fluid, will create streamwise fluctuations that lead to isotropic turbulence regions with important consequences for mixing and transport flux. We can infer that both the turbulent mixing and combustion rates could be enhanced using these mechanisms. The right choice of turbulence enhancing particles with the focus on the near-nozzle region shall affect the overall performance of the rocket engine and modify its exhaust content. The two-way global and local coupling mechanisms could not be neglected in numerical simulations and analytical models of multi-phase rocket engines.

References

S. Balachndar, J. K. Eaton, Turbulent dispersed multiphase flow, Annu. Rev. Fluid Mech. 42 (2010) 111–133.

J. D. Kulick, J. R. Fessler, J. K. Eaton, Particle response and turbulent modification in fully developed channel flow, J. Fluid Mech. 277 (1994) 109–134.

J. Kussin, M. Sommerfeld, Experimental studies on particle behaviour and turbulence modification in horizontal channel flow with different wall roughness, Exp. Fluids 33 (2002) 143–159.

K. T. Kiger, C. Pan, Suspension and turbulence modification effects of solid particulates on a horizontal turbulent channel flow, J. Turb. 3 (2002) 1–21.

J. Li, H. Wang, Z. Li, S. Chen, C. Zheng, An experimental study on turbulence modificion in near-wall boundary layer of dilure gas-particle channel flow, Exp. Fulids 53 (2012) 1385– 1403.

M. Cisse, H. Homann, J. Bec, Slipping motion of large neutrally buoyant particles in turbulence, J. Fluid Mech. 735 (2013).

G. Hetsroni, Particles turbulence interactions, J. Multiph. Flow 15 (1989) 341–351.

T. Tanaka, J. K. Eaton, Classification of turbulence modification by dispersed spheres using novel dimensionless number, Phys. Rev. Lett. 101 (2008) 297–285.

Y. Meller, A. Liberzon, Particle–fluid interaction forces as the source of acceleration PDF invariance in particle size, Int. J. Multiph. Flow 76 (2015) 22 – 31.

C. T. Crowe, J. D. Schwarzkopf, M. Sommerfeld, Y. Tsuji, Multiphase Flows with Droplets and Particles, CRC Press, 2011.

R. A. Gore, C. T. Crowe, Effect of particle size on modulating turbulent intensity, Int. J Multiph. Flow 15 (1989) 279–285.

A. Gany, L. Caveny, M. Summerfield, Aluminized solid propellants burning in a rocket motor flow field, AIAA 16 (1978) 736–739.

L. H. Caveny, A. Gany, Breakup of Al/Al_2O_3 agglomerates in accelerating flowfields, AIAA 17 (1979) 1368–1371.

F. Prevost, J. Boree, H. J. Nuglisch, G. Charnay, Measurements of fluid/particle correlated motion in the far field of an axisymmetric jet, Int. J. Multiph. Flow 22 (1996) 685–701.

M. Elhimer, O. Praud, M. Marchal, C. Cazin, R. Bazile, Simultaneous PIV/PTV velocimetry technique in a turbulent particle-laden flow, J. Visual. 20 (2017) 289–304.

C. Poelma, J. Westerweel, G. Ooms, Turbulence statistic from optical whole-field measurements in particle-laden turbulence, Exp. Fluids 40 (2006) 347–363.

D. A. Khalitov, K. Longmire, Simultaneous two-phase PIV by two-parameter phase discrimination, Exp. Fluids 32 (2002) 252–268.

W. Hwang, J. K. Eaton, Homogeneous and isotropic turbulence modulation by small heavy ($St \approx 50$) particles, J. Fluid Mech. 564 (2006) 361–393.

K. N. Volkov, V. N. Emel'yanov, I. V. Kurovs, Flow and motion of condensed-phase particles in the prenozzle space on solid-propellant rocket motors, J. Eng. Phys. Thermophys. 85 (2012) 724–731.

A. Ciucci, G. Iaccarino, Numerical analysis of the turbulent flow and alumina particles in solid rocket motors, J. Eng. Phys. Thermophys. 85 (2012) 1–15.

OpenPIV, OpenPIV/OpenPIV-Python, 2019. URL: `https://doi.org/10.5281/zenodo.3566451`. doi:10.5281/zenodo.3566451.

H. Wadell, Volume, shape and roundness of rock particles, J. Geology 40 (1935) 443–451.

N. A. Riley, Projection sphericity, J. Sediment. Petrology 11 (1941) 94–97.

Y. Hardalupas, A. M. K. P. Taylor, J. H. Whitelaw, Velocity and particle-flux characteristics of turbulent particle-laden jets, Proc. Royal Soc. A. 426 (1989) 31–78.

S. Elghobashi, G. C. Trusedell, On the two-way interaction between homogeneous turbulence and dispersed solid particles. I: Turbulence modification, Phys. Fluids 5 (1993) 177–216.

M. Esmaily, J. Horwitz, Investigation of a four-way coupling regime using a corrected point-particle approach, Annual Research Brief (2017) 49–62.

M. Gilbert, L. Davis, D. Altman, Velocity lag of particles in linearly accelerated combustion gases, J. Jet Prop. 25 (1955) 26–30.

M. Shah, M. Tachie, PIV study of turbulent flow in asymmetric converging and diverging channels, Trans. ASME, Journal of Fluids Engineering 130 (2008) 011204–1.